PROCEEDINGS OF SCIENCE

Modulating electrons and phonons in two-dimensional silicon nanostructures

---

R.Q. Zhang[1]
City University Hong Kong
Department of Physics and Materials Science, Hong Kong SAR, China
E-mail: `aprqz@cityu.edu.hk`

Bolong Huang
City University Hong Kong
Department of Physics and Materials Science, Hong Kong SAR, China
E-mail: `bolhuang@cityu.edu.hk`

Low dimensional semiconducting nanomaterials offer promising applications in nanoelectronics, photovoltaics and thermoelectronics, facilitated by their large surface-to-volume ratio and quantum confinement effects. In particular, two-dimensional systems are unique in providing tunable electron and phonon behaviors for the application due to their anisotropic confinement and scattering. In this article, we review our work on the modulation of electrons and phonons in two-dimensional silicon nanostructures which were explored via quantum-mechanical and atomistic level calculations. Our results include anisotropic energy band and optical properties of silicon sheet, energy band engineering through straining, and thermal conductivity modulation by vacancies of the various two-dimensional silicon nanostructures.

2013 International Workshop on Computational Science and Engineering (IWCSE 2013)
October 14-17, 2013
Taipei, Taiwan

---

[1] Speaker

1. Introduction

Silicon is the corner stone of the semiconductor industry. Silicon-based semiconducting materials have been exploited in numerous applications for its significant physical properties. With the continued trend for miniaturization of electronic devices, the low-dimensional silicon (Si) nanomaterials have attracted great attention from the scientific community due to their promising properties for electrical and electronic application. As a result, they have gradually become well admitted core components of contemporary electronic devices and technologies. Nowadays, various silicon nanostructures, such as nanowires and nanoribbons, with controllable sizes and morphologies, have been synthesized using different methods[1-6]. Moreover, the low-dimensional Si nanomaterials also offer themselves as either model systems or simulating prototypes for probing into the subtle relationships between structures and properties by both experimental and theoretical approaches.

As the silicon-based materials shrink down to the nanoscale, manifold interesting changes show up: the indirect band gap of the semiconductor gradually transforms itself into a direct band gap, the energy band gap widens, and the surface to volume ratio increases. The sum-total of the unprecedented bonuses accruing from the downsizing of Si-based materials is commonly known as quantum size effect or quantum confinement effect[6, 7]. The significant increase in the surface area with the down-scaling of materials provides plenty of room for functionalization of the surface. Consequently, to modulate the electronic properties of low-dimensional Si nanomaterials relies on strong interplays between the quantum confinement effects and nanosized structural variation, as can be found by experimental techniques.

As accumulated benefits from technology, we see that the recently synthesized two-dimensional (2D) Si nanomaterials[8, 9] bridge the gap between the one-dimensional (1D) Si nanowires (SiNWs)[6, 10] and three-dimensional (3D) Si bulk crystal materials, but also inherit the subtle quantum effects following zero-dimensional (0D) Si quantum dots (SiQDs)[11] and 1D SiNWs. These low-dimensional Si nanotructures exhibit diverse electronic properties, due to quantum confinement in different dimensions, and have drawn the attention of the scientific community for extensive investigations. Thus, it is necessary that we lay out the characteristics of 0D and 1D Si nanomaterials for the reference of furthering on the studies of 2D Si nanosheets (SiNS).

On the other hand, the low-dimensional Si nanomaterials have rightfully received significant consideration in wide range of application. For instance, SiQDs can be used as the light-emitting diode (LED)[12, 13] and optimized tandem solar cell by effectively tuned band gap[14]. For SiNWs, such quasi 1D nanostructures result in the electronic carriers to be confined in the two directions perpendicular to the wire axis. They can be either indirect or direct band gaps depending on the growth orientation and diameter. The quantum size effect leads the band gap gradually increases along with the SiNWs diameter decreases[6, 7]. Especially for very thin SiNWs, the optical properties are significantly modified by quantum confinement, as the dielectric function exhibits strong anisotropy and new low-energy absorption peaks start to appear in the imaginary part of the dielectric function for polarization along the wire axis. Moreover, the SiNWs show visible and near-infrared photoluminescence

(PL) at room temperature with increases in band gap from 1.1 eV for 7 nm to 3.5 eV for 1.3 nm, indicating the large feasibility of fabricating Si-based visible optical nanodevices[6, 15-17].

Since the past decade, much research interests have merged on the structures and properties of 2D materials in the field of nanomaterials, especially after the development of free-standing single layer graphite (graphene) by the easiest preparation (mechanical exfoliation)[18]. With advanced nanotechnology, the layered nanostructures of silicon with atomic thickness (often called nanosheet) have been successfully synthesized[8, 9, 19, 20]. Very recently, the silicon nanoribbons grown eptaxially on silver (110) and (100) surfaces paved the way for the synthesis of graphene-like silicon nanosheets[21-23].

As we known, single-layered silicon sheets of different orientations are considered as the simplest models of two-dimensional silicon materials to study their electronic, optical, and thermal properties. Compared with silicon atomic chains, we found that the geometric character of silicon sheets has a great effect on the electronic, optical, and thermal properties, which provides a valuable understanding of the transition from one-dimensional to two-dimensional materials. In particular to the electronic structure, the direct gap in the one-dimensional structure could be maintained in the two-dimensional structure. In the following review, one of the studies is subject to the anisotropic electronic band structures and optical properties. The strain induced variation has been also discussed, showing the possibility of the extrinsic modulation of the electronic structures of 2D Si systems. Another concern is about the thermal properties and transportations of the 2D SiNS, as this give rise to the attention of the crucial implications for silicon-based thermal logic circuits as well as thermoelectric applications.

2. Strain induced band dispersion engineering in Si nanosheets

The application of external strain has lately been found to be one of the most promising tunable variables for modulating and developing high-performance nanoscale device, especially for Si nanosheets. Recently, strain has been used to enhance mobility in planar Si metal-oxide semiconductor field-effect transistors[24]. Herein, we explore the possibility of using strain to manipulate the electronic band structures of Si nanosheets, while focusing on its most widely investigated (100) and (110) facets. The study indicates that strain can tune not only the magnitude of the band gap but also the band dispersion (i.e., direct or indirect band gap), which has crucial implications for the applications of Si nanosheets in opto-electronics, luminescence, and solar cells. To model such effects, we constructed Si nanosheets with the thinnest Si layers in the periodic supercells were decoupled by a vacuum thickness larger than 15 Å. The (100) Si nanosheet contains three Si layers with a thickness of 2.58 Å, while the (110) Si nanosheet comprises two Si layers with thickness of 1.88 Å.

The application of tensile and compressive axial strains were first-principally simulated by scaling the lattice constant along the two mutually perpendicular directions of the nanosheet, and this method has been successfully used to study the strain effects on nanowires[25-30]. A considerably large strain studied in theoretical calculations[31] may not be easily realizable in experiments. However, the trend predicted by first principles calculations will facilitate a clearer understanding of the underlying physics, which in turn will support the related experiments.

We have first characterized the geometries of Si nanosheets free from any strain. The dangling bonds on the surfaces of silicon nanosheets of the (100) and (110) facets were fully terminated by hydrogen. The (100) and (110) Si nanosheets have D_{2d} and D_{2h} symmetries, respectively, and therefore, the size is initially set to $a_x = a_y = 3.84$ Å for the (100) Si nanosheet, and $a_x = (2)^{1/2}a_y$, $a_y = 5.43$ Å, for the (110) Si nanosheet. Then, we have performed a series of calculations of the total energy with different lattice constants for a given nanosheet, and the in-plane lattice constants were obtained at the equilibrium, ground state of the system, corresponding to the minimum in its total energy. This method has already been validated for the study of the strain effects[31]. The calculated in-plane lattice constants of both Si nanosheets are found to be greater than the initial input. For example, $a_x = a_y = 4.07$ Å were obtained for the (100) Si nanosheet. This indicates the expansion of the nanosheet perpendicular to the *xy* plane containing the nanosheet (i.e., the *z* direction), and this phenomenon is also observed in nanowires (NWs)[29, 30, 32].

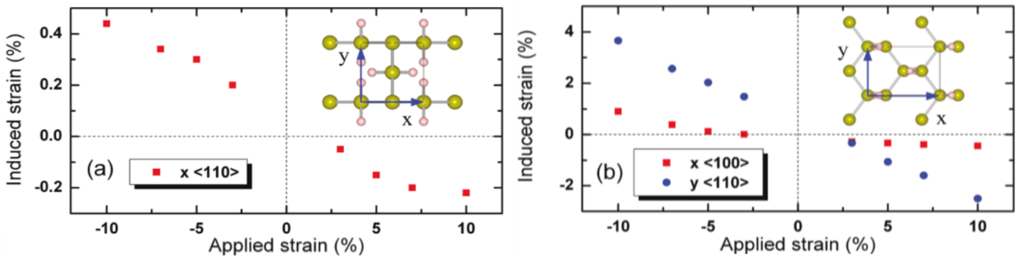

Figure 1. Induced strain as a function of applied strain for the (a) (100) Si nanosheet and the (b) (110) Si nanosheet. The insets are the ball and stick models representing the atomic arrangement where the big and small spheres denote silicon atoms and hydrogen atoms, respectively [35]. *Reprinted with permission from ref.[33] [C. Zhang, A. De Sarkar, and R. Q. Zhang, J. Phys. Chem. C 115, 23682 (2011)]. Copyright 2011, The American Chemical Society.*

As seen from the structure, the (100) Si nanosheet is stretchable along two equivalent <110> directions. Consequently, there exist two modes for applying axial strain on it: (i) symmetrical strain along the *x* and *y* directions and (ii) asymmetrical strain along the *x* or *y* direction. When an asymmetrical strain is applied to the Si nanosheet along *x*, the nanosheet will contract along the y direction. Along the x direction, the ratio of the changed lattice constant to the strain-free, optimized lattice constant refers to the applied strain. For a fixed lattice constant along the *x* direction, a series of total energy calculations have been performed using different lattice constants along the y direction. Along the *y* direction, the lattice constant corresponding to the energy minimum refers to the changed lattice constant, and its ratio to the strain-free lattice constant is termed as the induced strain. Figure 1(a) shows the induced strain as a function of strain applied to the (100) Si nanosheet. When subjected to the same degree of applied strain, the nanosheet is found to be more sensitive to compressive strain than to tensile strain. For example, a +5% (-5%) applied strain induces -0.15% (0.3%) strain. This implies that the (100) Si nanosheet is relatively readily compressible along the <110> direction, as compared to the other direction.

The modes of applying strain to the (110) Si nanosheet are different from that of the (100) Si nanosheet, due to the two nonequivalent directions. The structure sensitivity of the (110) Si nanosheet to the strain application along the <100> and <110> directions is shown in Figure

1(b). The applied strain along the <110> (y) direction induces a much larger strain. In particular, 10% of the compressive strain along the <110> direction induces 3.7% expansion along the <100> direction, the largest induced strain. Similar to the (100) Si nanosheet, applied compressive strain induces a larger strain. For example, a +5% asymmetrical strain applied along the y direction induces -1.1% strain, but a +5% asymmetrical strain applied along the x direction can produce only -0.33% induced strain. It may be inferred from these results that the (110) Si nanosheet is more sensitive to the application of compressive stress along the <110> direction.

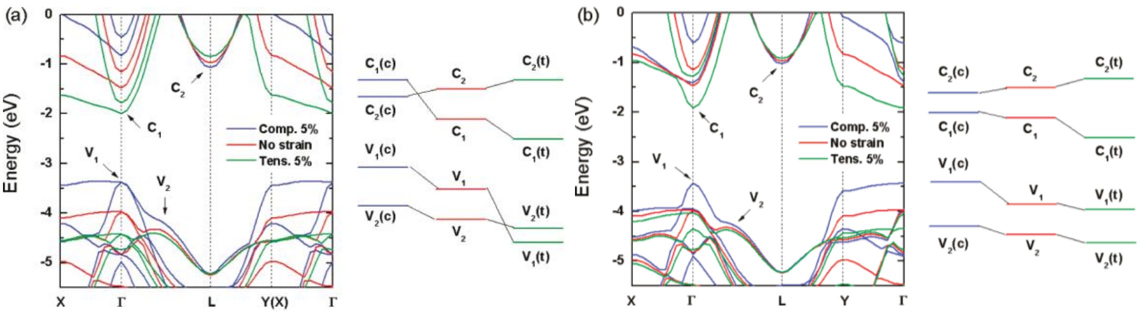

Figure 2. Electronic band structure (left panel) and schematic description of the evolution of energy states (right panel) of the (100) Si nanosheet under (a) symmetrical strain and (b) asymmetrical strain. The c and t in parentheses denote compressive and tensile strains, respectively. *Reprinted with permission from ref.[33] [C. Zhang, A. De Sarkar, and R.-Q. Zhang, J. Phys. Chem. C 115, 23682 (2011)]. Copyright 2011, The American Chemical Society.*

Figure 2 shows both the symmetric and asymmetric strain dependences of the electronic band structure of the (100) Si nanosheet. The shape and high symmetry points of the Brillouin zone can be found in our previous paper[34]. As the light emission or absorption of silicon-based nanostructures depends strongly on the band gap, we have labeled the energy states in Figure 2, which crucially determine the band gap, such as C_1 for the energy state at the conduction band edge. The energy states at point Y show a behavior similar to that at point Γ under strain, but they do not play a dominant role in the band gap transition and are therefore omitted in the following discussion. When no strain is applied to the (100) Si nanosheet, the energy differences between V_1 and V_2 ($\Delta V = V_1$-V_2) and the same between C_1 and C_2 ($\Delta C = C_2$-C_1) are 0.36 and 0.50 eV, respectively. It is noted here that a positive value of ΔV (ΔC) implies that the energy V_1 (C_2) is higher than V_2 (C_1). If both ΔV and ΔC are positive, a direct band gap is favored for the (100) Si nanosheet.

As we known, the direct band gap enhances the optical efficiency of Si devices (i.e., light absorption/emission), and consequently, it has potential for opto-electronic applications. When symmetrical compressive strain is applied to the (100) Si nanosheet, the C_1, V_1, and V_2 states rise in energy, while the C_2 state drops energetically. When the compressive strain is large enough to induce a negative ΔC value, the Si nanosheet undergoes a direct-to-indirect transition. Contrary to the compressive strain effect, the C_1, V_1, and V_2 states are downshifted in energy when symmetrical tensile strain is applied to the Si (100) nanosheet. Interestingly, the magnitude of the downward shift of V_1 is much larger than that of V_2, yielding a negative ΔV.

On the basis of these, it can be concluded that both symmetrical compressive and tensile strains can easily alter the electronic band dispersion of the (100) Si nanosheet from a direct band gap to an indirect band gap.

The effect of asymmetrical strain on the band structure of the (100) Si nanosheet is different from that of the symmetrical strain. Similar to the case of symmetrical compressive strain, the C_1, V_1, and V_2 states are shifted up in energy, while the C_2 state is downshifted. However, the extent of the upward shift of the C_1 state is small, leading to a positive ΔC, such as 0.38 eV at 5% compressive strain. Thus, the (100) Si nanosheet preserves the direct band gap up to 10% compressive strain. When asymmetrical tensile strain is applied to the Si nanosheet along the <110> direction, all of these involved energy states show totally different behaviors, leading to positive values for both ΔC and ΔV. Thus, within our studied range of applied strain, we observe that the application of asymmetrical compressive strain retains the direct band gap dispersion of the (100) Si nanosheet, while the tensile strain enhances the direct band gap.

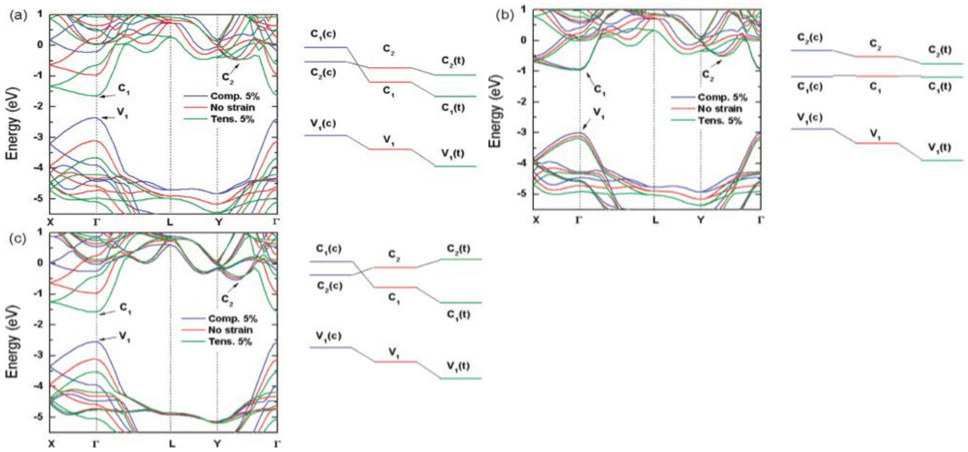

Figure 3. Electronic band structure (left panel) and schematic representation of the evolution of energy states (right panel) of the (110) Si nanosheet under (a) symmetrical strain and (b) asymmetrical strain along the x direction and (c) asymmetrical strain along the y direction. The c and t in parentheses denote compressive and tensile strains, respectively. *Reprinted with permission from ref.[33] [C. Zhang, A. De Sarkar, and R.-Q. Zhang, J. Phys. Chem. C 115, 23682 (2011)]. Copyright 2011, The American Chemical Society.*

When the (110) Si nanosheet is free from strain, both the valence band (V_1) maximum and conduction band (C_1) minimum located at point Γ, show a direct band gap. Under strain, a state in the conduction band, labeled as C_2, participates in the direct-to-indirect band gap transition. The schematic strain dependences of these three energy states and the electronic band structure of the (110) Si nanosheet are shown in Figure 3. The behaviors of V_1 under symmetrical and asymmetrical strains are identical, as shown in the right panel of Figure 2. The energy of the V_1 state increases when subjected to compressive strain, while it decreases under tensile strain, similar to the V_1 behavior in the (100) Si nanosheet. The C_2 energy state shows weak strain dependence, regardless of whether it is tensile or compressive strain. Thus, the other conduction band energy state, C_1 located at the Γ point, dominates the band gap characteristic. When symmetrical compressive strain is applied to the (110) Si nanosheet, the energy of C_1 rises. The value of ΔC becomes negative under sufficient compressive strain. As a result, the (110) Si nanosheet experiences a direct-to-indirect band gap transition. Contrary to the effect of compressive strain, the energy of the C_1 state decreases remarkably under symmetrical tensile strain, enlarging the direct band gap and its characteristics.

Interestingly, the energy of the C_1 state scarcely changes under asymmetrical strain along the *x* direction. The (110) Si nanosheet not only preserves the direct band gap characteristic but also shows amazing properties under asymmetrical strain. The detailed band gap evolution under asymmetrical strain is discussed hereafter. Under asymmetrical strain along the *y* direction, the electronic band structure of the (110) Si nanosheet is similar to that under symmetrical strain. The compressive strain induces a negative ΔC, and the tensile strain contributes positively to ΔC, enhancing the direct band gap.

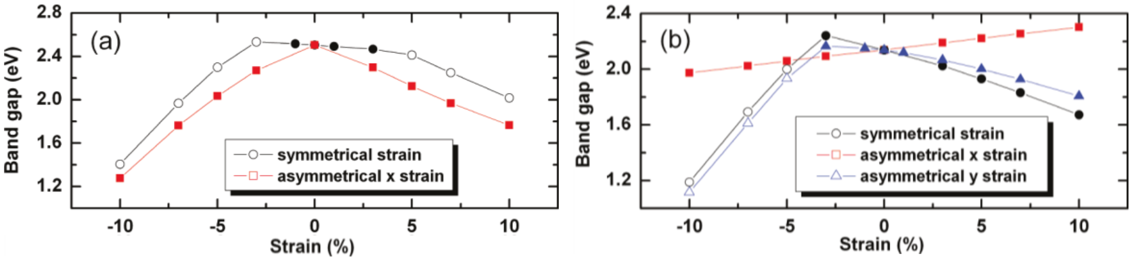

Figure 4. Band gap versus strain for (a) the (100) Si nanosheet and (b) the (110) Si nanosheet. Filled and unfilled symbols denote the direct and indirect band gaps, respectively. *Reprinted with permission from ref.[33] [C. Zhang, A. De Sarkar, and R.-Q. Zhang, J. Phys. Chem. C 115, 23682 (2011)]. Copyright 2011, The American Chemical Society.*

Figure 4 shows clearly the strain tunability of the band gap of Si nanosheets. To obtain a smaller band gap, a larger strain (at least 5%) needs to be applied to the (100) Si nanosheet, as shown in Figure 4(a). By carefully controlling the magnitude of the applied symmetrical compressive strain to the (100) Si nanosheet, a blue-shift followed by a red shift of the spectrum can be induced in photoluminescence measurements. This owes its origin to the rise in energy of the C_1 state. To have a direct band gap in optical and luminescence applications, asymmetrical strain along the x direction, as shown in Figure 4(a) by filled squares, will have to be applied.

The variation of the band gap of the (110) Si nanosheet with strain is shown in Figure 4(b). Interestingly, the magnitude of the direct band gap of the (110) Si nanosheets increase monotonically and linearly with asymmetrical strain along the *x* direction. On the basis of this behavior, one can get a larger band gap by applying tensile strain and a smaller gap by compressive strain. The unique band gap dependence accrues mainly from the C_1 energy state, whose energy remains almost nearly constant under asymmetrical strain along *x*. The smaller band gaps of direct type can also be obtained by applying symmetrical tensile strain and asymmetrical y tensile strain. Similar to the (100) Si nanosheet, a blue-shift followed by a red-shift will be observed in the spectrum, when symmetrical strain and asymmetrical compressive strain is consecutively applied along the y direction to the (110) Si nanosheet. This underscores the importance of strain engineering in Si nanosheets for applications in opto-electronics and luminescence. The external strain can be realized experimentally by controllable deposition or epitaxial growth methods. For instance, Kim et al.[9] have observed strain in their free-standing Si nanosheets and strain-induced variation in optical properties.

In conclusion, both (100) and (110) Si nanosheets have been found to be sensitive to compressive strain. For the same magnitude of applied strain, compressive strain produces a larger induced strain than that of the applied tensile strain. The (110) Si nanosheet is easier to be compressed along the <110> direction. The (100) Si nanosheet undergoes a direct-to-indirect band gap transition under sufficient symmetrical strain and preserves a direct band gap characteristic up to a 10% asymmetrical strain. Under asymmetrical strain along <100>, the direct band gap of the (110) Si nanosheet shows a linear relationship with the strain, which is a unique property advantageously exploitable in luminescence applications and opto electronic devices. The (110) Si nanosheet shows similar behavior when it is subjected to symmetrical and asymmetrical strain along <110>.

3. Thermal properties of silicon nanosheets

At the same time, a great research effort has been directed toward the electronic and thermal transport properties of silicon nanostructures to explore thermoelectric-related applications, where low thermal but high electronic conductivity of materials is required to obtain high thermoelectric efficiency. Our previous theoretical studies[25, 33-37] revealed that surface passivation and strain engineering can effectively tune the electronic band structure of silicon nanowires (SiNWs) and SiNSs; remarkable surface-transfer doping is also found in SiNWs. In addition, the thermal conductivity of SiNWs has been extensively studied both experimentally[38, 39] and theoretically[40-43]. The recent experimental breakthrough in SiNWs with ZT ~1 has benefited mainly from reduced phonon thermal conductivity via surface roughness[44]. Compared with 1D SiNWs, however, thermal transport in 2D SiNSs has not yet been cleared owing to the current difficulties experienced in synthesizing free-standing SiNSs[33].

Vacancy defects are unavoidable in nanostructures during growth and processing; furthermore, physical methods such as stress, irradiation, and sublimation can also lead to a considerable concentration of such defects[45, 46]. Recent studies have shown that such defects can lower phonon thermal conduction in both graphene[47] and SiNWs[48], but similar research is still scarcely reported in SiNSs. Here we perform equilibrium molecular dynamics (EMD) simulations to investigate the phonon thermal conductivity of graphene-like silicene sheets at 300K using the Green-Kubo method. We also explore the possibility of using vacancy defect engineering to reduce thermal transport in silicene and explain the underlying physical mechanism from the phonon spectral analysis. Our simulations clearly demonstrate that vacancy defects significantly influence not only the magnitude but also the anisotropy of thermal conductivity, which has crucial implications for thermal-related applications of SiNSs.

In contrast to graphene with a planar hexagonal structure owing to C-C sp2 hybridization, the larger Si-Si inter-atomic distance and p-orbital splitting weaken the π-π overlaps. Thus, it is unable to maintain the planar structure in free-standing silicene sheets, resulting in a low-buckled stable structure with sp3-like hybridization, which has been confirmed in theory[49, 50] and in recent experiments, similar to the silicon (111) layer[34]. Figure 5 shows the energetically favored geometry of an isolating silicene with an initial unrelaxed square cell.

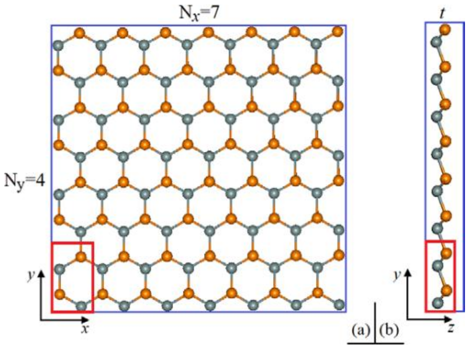

Figure 5: (Colour on-line) The hexagonal lattice structure of a silicene sheet with an unrelaxed square cell from (a) the top view and (b) the side view, respectively. The area enclosed by the red line represents the primitive cell. The blue lines denote the boundary of the simulation domain. *Reprinted with permission from ref.[51] [H. P. Li and R. Q. Zhang, EPL 99, 36001 (2012)]. Copyright 2012, IoP.*

Requiring no a priori understanding of the detailed phonon processes, an EMD simulation combined with the Green-Kubo formula is known to be effective in predicting the lattice thermal conductivity of nanomaterials[40]. In this scheme, EMD is used to calculate the heat current from the displacements, velocities, and forces for the atoms at each time step; the Green-Kubo formula is then used to calculate thermal conductivity from integrating the heat current autocorrelation function (HCACF), written as

$$\kappa_\alpha = \frac{1}{Vk_B T^2}\int_0^\infty \langle J_\alpha(0)\cdot J_\alpha(t)\rangle dt,$$

where V is the system volume, k_B is the Boltzmann constant, T is the temperature, J_α is the α-component of the heat current which was previously defined in reference [43], and κ_α is the α-component of the thermal conductivity tensor. $\langle J_\alpha(0)\cdot J_\alpha(t)\rangle$ represents the HCACF. For the 2D systems of interest here on the *xy*-plane, the reported in-plane thermal conductivity $\kappa_{in-plane}$ is the average value of κ_x and κ_y. In our simulations, Tersoff's bond-order potential[52] is used to describe the many-body forces among silicon atoms.

We assign the initial velocity from a Gaussian distribution around 300 K. Newtonian equations of the particle motion are integrated using the velocity Verlet algorithm. Temperature is simply controlled using the velocity scaling method. The periodic boundary conditions are used in the in-plane x- and y-directions, while the free boundary condition is used for the out-plane z -direction. We first fully relax each initial structure for 250 ps to attain the equilibrated state at the constant volume and temperature of 300 K. Following equilibration, we continue constant energy simulations in the microcanonical (NVE) ensemble for up to about 6.0 ns to calculate the in-plane thermal conductivity from our integrated method based on the Green-Kubo formula. To reduce fluctuation, we calculate the thermal conductivities from at least six realizations with different initial conditions, and then average them to obtain a reliable value for each case. We adopt no quantum correction to thermal conductivity in our study, since we are focused only on the effect of vacancy defects on thermal conductivity at room temperature. To explain the phenomenon deduced from the simulations, we calculate the phonon density of states (PDOS) spectrum from the Fourier transform of velocity autocorrelation function[53].

Figure 6 depicts the calculated thermal conductivities κ_x, κ_y and $\kappa_{\text{in-plane}}$. We find that κ_x, κ_y and $\kappa_{\text{in-plane}}$ show similar variation trends as the system size increases. The converged result suggests that the simulation effectively includes the dominant contribution to thermal conductivity coming from the different phonon modes. Although silicene and graphene are both 2D hexagonal lattices and have similar electronic band structures[50], they display different thermal transport features. A recent experiment demonstrated that the thermal conductivity of suspended single-layer graphene is in the range of ∼3000–5000W/mK near room temperature[53], which is clearly above the bulk graphite limit of ∼2000W/mK. In contrast, for the silicene sheet, our simulation reveals its in-plane thermal conductivity to be about 20W/mK at room temperature, which is one order of magnitude smaller than the value for bulk silicon (150–200W/mK[54]).

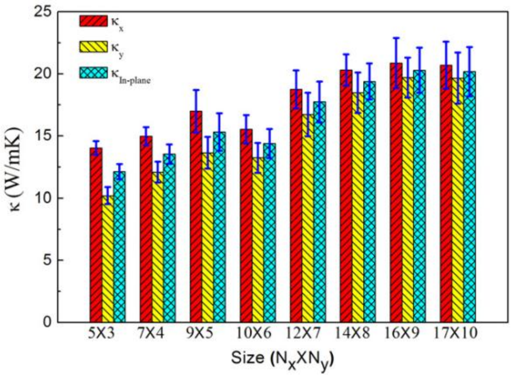

Figure 6. The simulation cell size effect on the thermal conductivities κx, κy and κin-plane for silicene square sheets, respectively. *Reprinted with permission from ref.[51] [H. P. Li and R. Q. Zhang, EPL 99, 36001 (2012)]. Copyright 2012, IoP.*

We next focus on the influence of vacancy defects on thermal transport in isolating a silicene sheet. To normalized thermal conductivity, the ratio between the in-plane thermal conductivity of the defective sheet (κ) and that of the pristine silicene sheet (κ_0), instead of to their absolute values. Figures 7 (a) and (b) plot normalized in-plane thermal conductivity against the concentration of monoatomic vacancies and the size of vacancy clusters, respectively. We find that even for the lowest monovacancy concentration ρ of 0.22% (i.e., one of the 448 atoms is removed), thermal conductivity reduction can be remarkable (by 78%) compared with a perfect case. As the vacancy sites increase to 0.45% and 1.56%, normalized in-plane thermal conductivity can be reduced to ∼ 0.50 and ∼0.28, respectively. Furthermore, when the vacancy concentration increases from 1.56% to 4.5%, the reduction in normalized in-plane thermal conductivity is only about 0.10. Fitting the simulation results in Figure 7 (a) also gives $\kappa/\kappa0 = 1/(1.166+1.529\rho)$ for monoatomic vacancies at 300 K, indicating a significant reduction in thermal conductivity below 2% in monovacancies, followed by a slow decrease in thermal conductivity at higher vacancy concentrations. In addition, we compute the thermal conductivity of silicene sheets with different-sized vacancy clusters, and find that vacancy clusters degrade thermal conductivity more remarkably than do monoatomic vacancies, as shown in Figure 7 (b). In particular, removing a 12-atom cluster decreases the thermal conductivity of a pristine sheet by half, while a monoatomic vacancy induces a reduction of about 78%. Increasing the size of a vacancy cluster thus results in a larger reduction in thermal conductivity owing to the stronger effect of phonon-defect scattering.

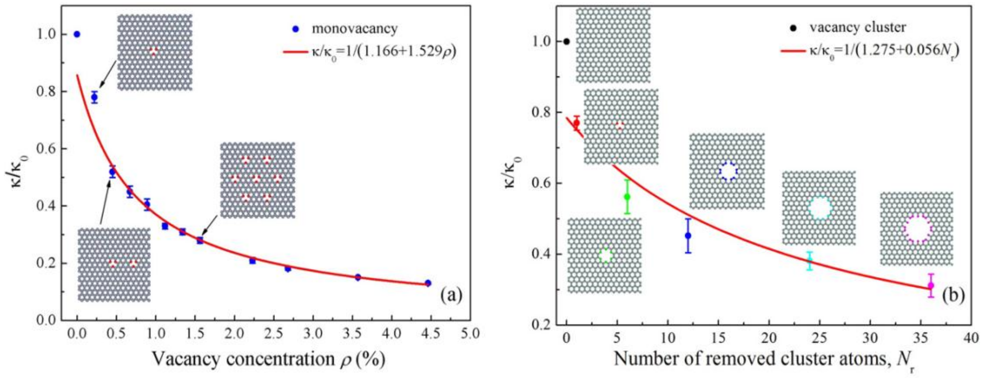

Figure 7. Normalized in-plane thermal conductivity (κ/κ0) of silicene sheets as a function of (a) the monoatomic vacancy concentration and (b) the number of cluster atoms removed. In the snapshots, the gray balls denote silicon atoms, while other coloured balls denote the edge atoms of the vacancies. *Reprinted with permission from ref.[51] [H. P. Li and R. Q. Zhang, EPL 96, 36001 (2012)]. Copyright 2012, IoP.*

To elucidate the reduction trend in thermal conductivity, we plot the in-plane PDOS spectral associated with vacancy defects in silicene sheets in Figure 8. Also plotted is the overall PDOS of bulk silicon for comparison. Phonon modes with frequencies below 20THz dominate the thermal transport in silicon[55], and our simulated PDOS for bulk silicon shows excellent agreement with the experimental and theoretical data[56]. Compared with bulk silicon, the in-plane PDOS for pristine silicene sheets exhibit a significant depression in the considered frequency region because of the effect of surface-phonon scattering. Additionally, our simulations reveal a shortening of the Si-Si bond for free surfaces owing to bond reconstruction[57]; thus, the stiffer surface bond could account for a significant shift in the entire PDOS to higher frequencies. The depression of the PDOS reduces the density of thermal energy carriers[58], while the blue-shift of a low-frequency PDOS may decrease the contribution of long-wavelength phonon modes dominating heat conduction at low temperature[55]. Both contribute directly to the reduction in thermal conductivity, as confirmed by our simulations.

The Figure 8 (a) and (b) show, by increasing the concentration of monovacancies or the size of the vacancy cluster, the high frequency parts of the PDOS near 18 THz are remarkably reduced, leading to lower thermal conductivity, since the optical modes could also carry some heat[42]. Also, we find a remarkable broadening of the acoustic phonon modes near 6 THz and

12.5 THz as vacancy concentration and hole size increase. Particularly in the case of larger contractions or the larger sized vacancy defects we study, the valleys and peaks in the PDOS curve between 10 and 16 THz almost disappear, and this part of the PDOS curve flattens. These show that the vacancies in a silicon nanosheet strongly scatter the phonons, and that this source of scattering is associated with the concentration and size of the vacancies.

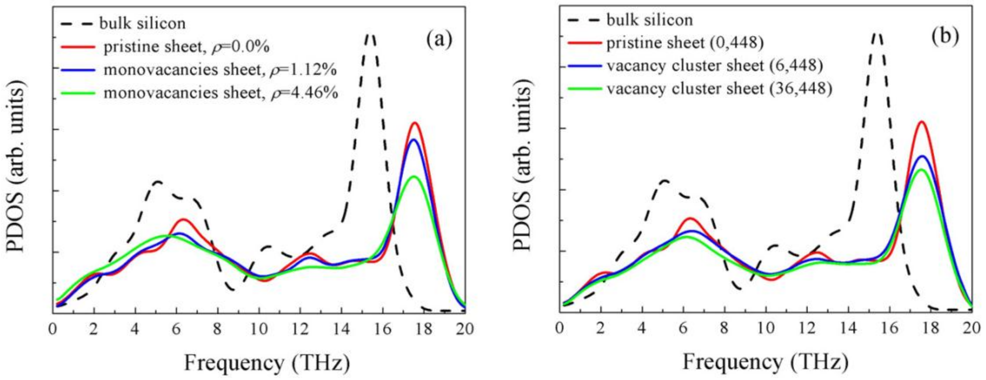

Figure 8. In-plane PDOS analysis of the effect of (a) the monoatomic vacancy concentration, and (b) the size of a vacancy cluster for a silicene sheet. Overall PDOS for bulk silicon is plotted by the dashed line for comparison. ρ is the concentration of monoatomic vacancies. (6,448) denotes that a 6-atom cluster was removed from a 448-atom cell, as illustrated by the snapshot in Figure 7(b). *Reprinted with permission from ref.[51] [H. P. Li and R. Q. Zhang, EPL 99, 36001 (2012)]. Copyright 2012, IoP.*

The boundary shape of the vacancy clusters also plays an important role in the thermal conductivity of silicene sheets. Figure 9 plots the normalized thermal conductivity and the thermal conductivity anisotropy ratio of silicene sheets with different vacancy clusters. We consider three types of clusters, namely, circular, triangular, and rectangular. Although the considered nanoholes show a similar area because the same number of silicon atoms has been removed, the number and arrangement of the boundary atoms are remarkably different. Since the vibrational modes near the hole boundary involve only few atoms, they are very sensitive to the surface/edge condition of the vacancy holes. Figure 6 shows that the heat transport along the zigzag and armchair directions in pristine square silicene is similar (for example, $\kappa_x/\kappa_y \sim 1.09 \pm 0.11$ for a 14×8 cell), indicating a quasi-isotropic thermal conductivity. But from Figure 9 we see significant anisotropy of thermal conductivity in the vacancy cluster sheet. In contrast to the circular and triangular vacancy clusters, the rectangular vacancy cluster has a stronger effect on thermal conductivity anisotropy because of the greater discrepancy in the vacancy-boundary length along the thermal transfer direction, resulting in the directional difference of the phonon-vacancy scattering ratio[59].

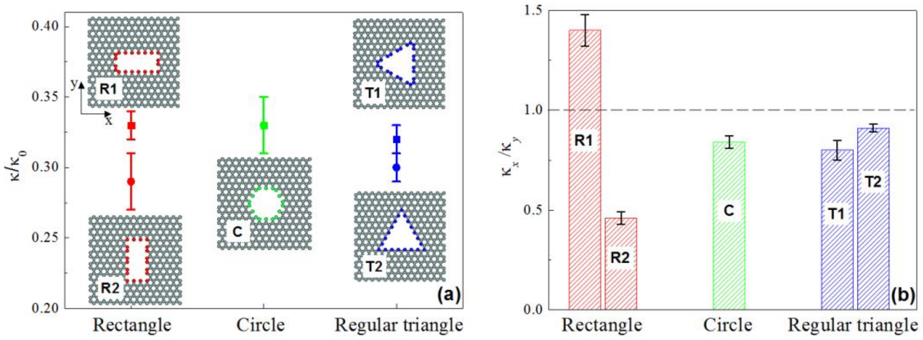

Figure 9. (a) Normalized in-plane thermal conductivity (κ/κ_0) and (b) thermal conductivity anisotropy ratio (κ_x/κ_y) of silicene sheets with different boundary shapes of vacancy clusters at 300 K. In the snapshots, the red, green, and blue balls denote the edge silicon atoms of rectangular vacancy clusters (R1, R2), a circular vacancy cluster (C), and regular triangular vacancy clusters (T1, T2), respectively. Here the vacancy clusters are formed by the removal of Si_{36} from the 14×8 cell with 448 atoms. κx/κy =1 corresponds to the pure isotropy of thermal conductivity. *Reprinted with permission from ref.[51] [H. P. Li and R. Q. Zhang, EPL 99, 36001 (2012)]. Copyright 2012, IoP.*

Through the investigation, the phonon spectrum and thermal conductivity of 2D silicene sheets differ dramatically from those of bulk silicon. The in-plane thermal conductivity of silicene sheets is about one order of magnitude lower than the bulk value. The structural defects such as vacancies and vacancy clusters contributes significantly to reducing thermal conductivity owing to the stronger effect of phonon-vacancy scattering, giving a method for tuning thermal transport in 2D systems. Moreover, the edge shape of vacancy clusters has a significant influence not only on the values of thermal conductivity, but also on its anisotropy (by increasing or decreasing the values in a specific direction); this is crucial for the chiral-angle tailoring of the thermal conductivity of silicene sheets.

4. Summary

We have reviewed anisotropic energy band and optical properties of silicon sheet, energy band engineering through straining, and thermal conductivity modulation by vacancies of the various two-dimensional silicon nanostructures. As seen from the study, the band structures of Si nanosheets can be manipulated to have different band gap characteristics by the application of different kinds of axial strains. With the simulations of thermal properties, the work reveals the importance of vacancy engineering in tuning thermal transport in low-dimensional silicon nanostructures. The findings have crucial implications for silicon-based thermal logic circuits as well as thermoelectric applications.

References

[1] R. S. Wagner and W. C. Ellis, Appl. Phys. Lett. **4**, 89 (1964).
[2] A. M. Morales and C. M. Lieber, Science **279**, 208 (1998).

[3] Y. F. Zhang, Y. H. Tang, N. Wang, D. P. Yu, C. S. Lee, I. Bello, and S. T. Lee, Appl. Phys. Lett. **72**, 1835 (1998).
[4] J. Westwater, D. P. Gosain, S. Tomiya, S. Usui, and H. Ruda, J. Vac. Sci. Technol. B **15**, 554 (1997).
[5] R. Q. Zhang, Y. Lifshitz, and S. T. Lee, Adv. Mater. **15**, 635 (2003).
[6] D. D. D. Ma, C. S. Lee, F. C. K. Au, S. Y. Tong, and S. T. Lee, Science **299**, 1874 (2003).
[7] X. Zhao, C. M. Wei, L. Yang, and M. Y. Chou, Phys. Rev. Lett. **92**, 236805 (2004).
[8] H. Nakano, T. Mitsuoka, M. Harada, K. Horibuchi, H. Nozaki, N. Takahashi, T. Nonaka, Y. Seno, and H. Nakamura, Angew. Chem. Int. Edit. **45**, 6303 (2006).
[9] U. Kim, I. Kim, Y. Park, K.-Y. Lee, S.-Y. Yim, J.-G. Park, H.-G. Ahn, S.-H. Park, and H.-J. Choi, ACS Nano **5**, 2176 (2011).
[10] Y. Cui, Q. Wei, H. Park, and C. M. Lieber, Science **293**, 1289 (2001).
[11] M. V. Wolkin, J. Jorne, P. M. Fauchet, G. Allan, and C. Delerue, Phys. Rev. Lett. **82**, 197 (1999).
[12] V. L. Colvin, M. C. Schlamp, and A. P. Alivisatos, Nature **370**, 354 (1994).
[13] V. I. Klimov, A. A. Mikhailovsky, S. Xu, A. Malko, J. A. Hollingsworth, C. A. Leatherdale, H.-J. Eisler, and M. G. Bawendi, Science **290**, 314 (2000).
[14] G. Conibeer, I. Perez-Wurfl, X. Hao, D. Di, and D. Lin, Nanoscale Res. Lett. **7**, 193 (2012).
[15] D. P. Yu, et al., Appl. Phys. Lett. **73**, 3076 (1998).
[16] J. Qi, J. M. White, A. M. Belcher, and Y. Masumoto, Chem. Phys. Lett. **372**, 763 (2003).
[17] A. R. Guichard, D. N. Barsic, S. Sharma, T. I. Kamins, and M. L. Brongersma, Nano Lett. **6**, 2140 (2006).
[18] K. S. Novoselov, A. K. Geim, S. V. Morozov, D. Jiang, Y. Zhang, S. V. Dubonos, I. V. Grigorieva, and A. A. Firsov, Science **306**, 666 (2004).
[19] H. Okamoto, et al., J. Am. Chem. Soc. **132**, 2710 (2010).
[20] Y. Sugiyama, H. Okamoto, T. Mitsuoka, T. Morikawa, K. Nakanishi, T. Ohta, and H. Nakano, J. Am. Chem. Soc. **132**, 5946 (2010).
[21] A. Kara, C. Léandri, M. E. Dávila, P. Padova, B. Ealet, H. Oughaddou, B. Aufray, and G. Lay, J. Supercond. Nov. Magn. **22**, 259 (2009).
[22] G. Le Lay, B. Aufray, C. Léandri, H. Oughaddou, J. P. Biberian, P. De Padova, M. E. Dávila, B. Ealet, and A. Kara, Appl. Surf. Sci. **256**, 524 (2009).
[23] B. Aufray, A. Kara, S. Vizzini, H. Oughaddou, C. Léandri, B. Ealet, and G. Le Lay, Appl. Phys. Lett. **96** (2010).
[24] B. M. Haugerud, L. A. Bosworth, and R. E. Belford, J. Appl. Phys. **94**, 4102 (2003).
[25] A. J. Lu, R. Q. Zhang, and S. T. Lee, Appl. Phys. Lett. **91** (2007).
[26] K.-H. Hong, J. Kim, S.-H. Lee, and J. K. Shin, Nano Lett. **8**, 1335 (2008).
[27] L. Huang, N. Lu, J.-A. Yan, M. Y. Chou, C.-Z. Wang, and K.-M. Ho, J. Phys. Chem. C **112**, 15680 (2008).
[28] P. W. Leu, A. Svizhenko, and K. Cho, Phys. Rev. B **77**, 235305 (2008).
[29] P. Logan and X. Peng, Phys. Rev. B **80**, 115322 (2009).
[30] X. H. Peng, A. Alizadeh, S. K. Kumar, and S. K. Nayak, Int. J. Appl. Mech. **1**, 483 (2009).
[31] G. Gui, J. Li, and J. Zhong, Phys. Rev. B **78**, 075435 (2008).
[32] X. Peng and P. Logan, Appl. Phys. Lett. **96** (2010).
[33] C. Zhang, A. De Sarkar, and R.-Q. Zhang, J. Phys. Chem. C **115**, 23682 (2011).
[34] A. J. Lu, X. B. Yang, and R. Q. Zhang, Solid State Commun. **149**, 153 (2009).
[35] B. K. Teo, S.-P. Huang, R. Q. Zhang, and W.-K. Li, Coordin. Chem. Rev. **253**, 2935 (2009).
[36] R. Q. Zhang, Y. Lifshitz, D. D. D. Ma, Y. L. Zhao, T. Frauenheim, S. T. Lee, and S. Y. Tong, J. Chem. Phys. **123** (2005).
[37] H. Xu, X. B. Yang, C. Zhang, A. J. Lu, and R. Q. Zhang, Appl. Phys. Lett. **98** (2011).
[38] D. Li, Y. Wu, P. Kim, L. Shi, P. Yang, and A. Majumdar, Appl. Phys. Lett. **83**, 2934 (2003).
[39] C.-Y. Chen, D. H. Phan, C.-C. Wong, and T.-J. Yen, J. Electrochem. Soc. **158**, D302 (2011).
[40] P. K. Schelling, S. R. Phillpot, and P. Keblinski, Phys. Rev. B **65**, 144306 (2002).
[41] X. Li, K. Maute, M. L. Dunn, and R. Yang, Phys. Rev. B **81**, 245318 (2010).
[42] M. Hu, X. Zhang, K. P. Giapis, and D. Poulikakos, Phys. Rev. B **84**, 085442 (2011).
[43] H. P. Li, A. De Sarkar, and R. Q. Zhang, EPL **96**, 56007 (2011).

[44] A. I. Hochbaum, R. Chen, R. D. Delgado, W. Liang, E. C. Garnett, M. Najarian, A. Majumdar, and P. Yang, Nature **451**, 163 (2008).
[45] V. C. Venezia, L. Pelaz, H.-J. L. Gossmann, T. E. Haynes, and C. S. Rafferty, Appl. Phys. Lett. **79**, 1273 (2001).
[46] X. Y. Cui, R. K. Zheng, Z. W. Liu, L. Li, B. Delley, C. Stampfl, and S. P. Ringer, Phys. Rev. B **84**, 125410 (2011).
[47] H. Zhang, G. Lee, and K. Cho, Phys. Rev. B **84**, 115460 (2011).
[48] K. Yamamoto, H. Ishii, N. Kobayashi, and K. Hirose, Applied Physics Express **4**, 085001 (2011).
[49] S. Cahangirov, M. Topsakal, E. Aktürk, H. Şahin, and S. Ciraci, Phys. Rev. Lett. **102**, 236804 (2009).
[50] C.-C. Liu, W. Feng, and Y. Yao, Phys. Rev. Lett. **107**, 076802 (2011).
[51] H.-P. Li and R.-Q. Zhang, EPL **99**, 36001 (2012).
[52] J. Tersoff, Phys. Rev. B **39**, 5566 (1989).
[53] S. Ghosh, W. Bao, D. L. Nika, S. Subrina, E. P. Pokatilov, C. N. Lau, and A. A. Balandin, Nat Mater **9**, 555 (2010).
[54] R. K. Kremer, K. Graf, M. Cardona, G. G. Devyatykh, A. V. Gusev, A. M. Gibin, A. V. Inyushkin, A. N. Taldenkov, and H. J. Pohl, Solid State Commun. **131**, 499 (2004).
[55] J. E. Turney, A. J. H. McGaughey, and C. H. Amon, J. Appl. Phys. **107** (2010).
[56] Z. Tang and N. R. Aluru, Phys. Rev. B **74**, 235441 (2006).
[57] D. K. Yu, R. Q. Zhang, and S. T. Lee, Phys. Rev. B **65**, 245417 (2002).
[58] W. Fon, K. C. Schwab, J. M. Worlock, and M. L. Roukes, Phys. Rev. B **66**, 045302 (2002).
[59] H. Karamitaheri, M. Pourfath, R. Faez, and H. Kosina, J. Appl. Phys. **110** (2011).